Available online at www.sciencedirect.com
ScienceDirect
Journal of Computational Physics 222 (2007) 673–701
JOURNAL OF COMPUTATIONAL PHYSICS
www.elsevier.com/locate/jcp

Explicit small-scale velocity simulation for high-*Re* turbulent flows. Part II: Non-homogeneous flows

K.A. Kemenov, S. Menon *

School of Aerospace Engineering, Georgia Institute of Technology, 270 Ferst Drive, Atlanta, Georgia 30332-0150, United States

Received 3 June 2006; received in revised form 12 August 2006; accepted 15 August 2006
Available online 9 October 2006

Abstract

Two level simulation (TLS) approach based on the explicit reconstruction of the small-scale velocity fields, is extended to study non-homogeneous turbulent flows on coarse grids. Assumptions needed for the simplified treatment of the 3D small-scale governing equation on lines are analyzed using DNS data of well-developed turbulent channel flow. Fully coupled simulations of turbulent channel flow and temporally developed mixing layers suggest that explicit accounting of the small-scale velocity in the large-scale equations allows to correctly predict the large-scale turbulent dynamics without using a concept of eddy-viscosity.
© 2006 Elsevier Inc. All rights reserved.

Keywords: Non-homogeneous turbulent flows; Large eddy simulation; Subgrid-scale modeling

1. Introduction

Practical computations of high Reynolds number turbulent flows are nowadays possible under framework of large eddy simulation (LES) – a turbulence modeling approach which uses less empiricism and, at the same time, captures more turbulent flow features than its simpler counterpart Reynolds averaged Navier–Stokes (RANS) equations approach. LES focuses on a study of evolution of the *resolved* turbulent velocity field. The resolved field is usually associated with the filtered velocity field, as introduced by Leonard [1], and defined by a convolution of a spatial filter $G(\mathbf{x}, \Delta)$ of a characteristic size Δ and the total velocity field $u_i(\mathbf{x})$. Detailed account of LES approach can be found in a recent book by Sagaut [2], as well as in reviews given by Meneveau and Katz [3] and Piomelli [4].

There have been significant advances in LES methodology over the last 30 years both in modeling of the effect of unresolved scales [5–9], and in practical numerical applications of LES to various simple [10–12], and quite complex flows [13,14]. Nevertheless, some unsettled conceptual questions concerning LES foundations and LES practical implementation do exist. Many of them were recently formulated by Pope as ''Ten Questions'' to LES of turbulent flows [15]. The first two questions: ''is LES the right approach?'' and ''Can the resolution of all

* Corresponding author. Tel.: +1 404 894 9126; fax: +1 404 894 2760.
E-mail addresses: kkemenov@gatech.edu (K.A. Kemenov), suresh.menon@ae.gatech.edu (S. Menon).

0021-9991/$ - see front matter © 2006 Elsevier Inc. All rights reserved.
doi:10.1016/j.jcp.2006.08.002

scales be made tractable?'' are intimately linked to inability of LES to treat flows where dynamically important processes are governed by scales smaller than Δ. Wall-bounded turbulent flows at high Reynolds number gives probably the most important example.

In an attempt to generalize applicability of LES to treat complex flows, the authors recently proposed two level simulation (TLS) approach [16]. TLS is a computational framework where the continuous large-scale (LS) and small-scale (SS) governing equations are introduced without use of filtering or LS separation operators. This allows to avoid (at least formally) the undesired commutation problem between differentiation and the LS separation operators, and extend the standard continuous LES equations to treat non-homogeneous flows without introducing extra non-commutation terms in the governing equations as well as the eddy viscosity. In TLS approach, the SS governing equations are simplified and treated on a collection of lines embedded in the three-dimensional flow domain. Such treatment results in tractable computations of the small scales while retaining full coupling between the LS and SS fields.

In the previous work [16], TLS approach was applied to forced homogeneous and isotropic turbulence. In this paper, we extend TLS further to simulate non-homogeneous turbulent flows. Two benchmark cases of such flows are considered: temporally evolving mixing layers and well-developed turbulent channel flow. While the former case gives an example of free shear turbulent flow, for which LES is a convincingly right approach, the latter wall-bounded case presents the well-documented challenges for LES due to severe near-wall resolution requirements at high Reynolds numbers. The most intense turbulent production events occur well into the *inner* layer [17] and control the transport processes in the whole flow. To avoid DNS like near-wall resolution [18], various near-wall modeling approaches have been proposed in literature (see an extensive review in [19]). While simple wall models provide more or less physically justifiable constraint on the wall shear stress [20–22], the more sophisticated wall models, referred as zonal or hybrid approaches, usually involve geometric decomposition of the flow field into inner and outer regions with subsequent introduction of special non-LES dynamic equations in the inner region.

In the two-layer model (TLM) proposed by Balaras et al. [23], a simplified set of the boundary layer equations was employed to model the inner layer motions while LES equations are solved in the outer region, away from the wall. Another hybrid approach – detached eddy simulation (DES) [24] exploits the idea of merging solution of unsteady RANS equations in the near-wall region with LES solution in the rest of flow. However, there exist some fundamental and practical difficulties related to merging of two conceptually different solutions, i.e., the time-averaged and the spatially filtered, at the interface of LES and RANS regions [25]. Major difficulties stem from the fact that the RANS type of solution usually lacks the small-scale motion close to the interface, which is required to provide the LES region with physically plausible level of turbulent fluctuations. This phenomenon probably manifests itself as the velocity mismatch between RANS and LES regions, which was first reported by Nikitin et al. [26] in DES of channel flows.

The topic remains to be an area of active research efforts and several different approaches have been proposed recently. Piomelli et al. [27] introduced stochastic forcing in the inner layer close to the interface which resulted in the improvement in prediction of the mean velocity. Adding extra forcing has been also considered by Benarafa et al. [28]. Hamba [29] studied effects of additional filtering at the interface and found it to be beneficial. No forcing approach was proposed by Temmerman et al. [25]. It utilizes the use of compatibility conditions for velocity and turbulent viscosity across the interface. Another conceptually different approach, which naturally introduces small-scale velocity fluctuations in the near-wall region, was developed by Schmidt et al. [30]. The approach employs the stochastic one-dimensional turbulence (ODT) model of Kerstein [31], which was incorporated into a set of the boundary layer equations and solved on wall-normal lines placed in the near-wall region. While all approaches showed improvement in prediction of the important statistical quantities, their generality and inevitable degree of arbitrariness, through the introduction of turbulent eddy viscosity and tunable model parameters, remain subjects for continuing research efforts.

In this context, TLS approach can potentially present a useful alternative since it does not require introduction of the interface, and does not rely on the concept of eddy viscosity. While all hybrid zonal approaches use some form of domain (geometrical) decomposition, in TLS the functional decomposition is induced through representation $u_i = u_i^L + u_i^S$. In other words, both the LS and the SS fields are assumed to exist in the near-wall region and evolve according to their own governing equations. In TLS approach the SS velocity field is reconstructed based on the known LS velocity field, by solving the simplified SS equations on lines. It is not claimed,

however, that such a coupled consideration of the LS and the SS fields would completely eliminate the need for an adequate LS resolution in the near-wall region. The role of the LS velocity field and its gradient is still important along with the range of scales they represent. The purpose of performing explicit SS simulation on lines in the near-wall region is two-fold: one is to relax the LS resolution requirement; and the other is to try, at least partially, to make the resolution of the SS tractable.

Explicit accounting for the SS fields distinguishes TLS approach from another class of alternative LES methods which are focused on solving the underresolved Navier–Stokes equations adopting non-linear regularization techniques. Extending the spectral viscosity concept of Tadmor [32] to incompressible turbulent flows, Karamanos and Karniadakis [33] developed the spectral vanishing viscosity (SVV) approach using modification of the viscous term, and demonstrated applicability of the method to treat wall-bounded flows. A dynamic version of the SVV method was further formulated by Kirby and Karniadakis [34] and successfully applied to simulate turbulent channel flow on coarse grids. In similar monotone integrated LES (MILES) approach, implicit regularization of the LS solution is achieved by careful prescription of high-order monotonicity preserving discretization schemes for the convective fluxes [35]. This is usually done by employing non-linear flux limiters in the convective flux reconstruction, which is equivalent to introduction of additional diffusion terms into Navier–Stokes equations [33,35]. A recent account of the MILES approach and its application to wall-bounded and free shear turbulent flows was discussed by Grinstein and Fureby in [36].

The objective of the present study is to demonstrate general applicability of TLS approach for two physically different cases of non-homogeneous turbulence: well-developed channel flow and temporally evolving mixing layers. For the latter, LES approach is quite successful, for the former it does not. Brief presentation of TLS governing equations are given in Section 2, full details are given elsewhere [16]. In Section 3, we revisit assumptions needed for simplified treatment of the SS equation on lines by conducting *a priori* analysis of non-homogeneous turbulence data taken from DNS of well-developed turbulent channel flow. Section 4 presents the results of TLS simulation of turbulent channel flow at $Re_\tau = 590$ based on the friction velocity, and the temporal mixing layers at $Re_\omega = 468$ based on the initial vorticity thickness. Conclusion and future recommendations are given in Section 5.

2. TLS governing equations

Using notation adopted in our previous work [16], TLS governing equations are represented by a coupled system of the LS and the SS equations, denoted as $G_i^L = 0$ and $G_i^S = 0$, respectively. These equations define evolution of the LS (u_i^L, p^L) and the SS (u_i^S, p^S) fields, and can be written for a case of the uniform density, incompressible flow as

$$G_i^L \equiv \frac{\partial u_i^L}{\partial t} + \frac{\partial}{\partial x_j}\left[(u_i^L + u_i^S)(u_j^L + u_j^S)\right]^L + \frac{\partial p^L}{\partial x_i} - \nu\frac{\partial^2 u_i^L}{\partial x_j^2} = 0 \tag{1}$$

$$G_i^S \equiv \frac{\partial u_i^S}{\partial t} + \frac{\partial}{\partial x_j}\left[(u_i^L + u_i^S)(u_j^L + u_j^S)\right]^S + \frac{\partial p^S}{\partial x_i} - \nu\frac{\partial^2 u_i^S}{\partial x_j^2} = 0 \tag{2}$$

The LS and SS velocities are also subject to the incompressibility constraint:

$$\frac{\partial u_i^L}{\partial x_i} = 0, \quad \frac{\partial u_i^S}{\partial x_i} = 0 \tag{3}$$

Moreover, the LS and SS fields are complements of each other, and form the total field according to the decomposition:

$$u_i^S + u_i^L = u_i, \quad p^S + p^L = p \tag{4}$$

Such a continuous representation of the LS $(\mathscr{F}^L)$ and the SS $(\mathscr{F}^S)$ fields depends on the minimal resolvable turbulent scale $\Delta(x)$, or on the maximum resolvable grid mode k_Δ, which can be associated with a certain discrete LS grid G^Δ such that the energy content of the LS field and its derivatives decays *sufficiently* fast beyond the maximum resolvable grid mode k_Δ [16]. The SS field is then defined as the relative complement of the LS field according to Eq. (4).

The rationale behind considering a system of Eqs. (1) and (2) (assuming that the LS and SS solutions exist) is three-fold.

(i) It gives a *sufficient* condition that the sum $u_i^S + u_i^L$ satisfies the Navier–Stokes equations $G_i^L + G_i^S = 0$.
(ii) The LS and SS equations provide natural two-way coupling between the LS and SS fields because of the presence of the LS or SS parts of the non-linear terms at the left hand sides of both equations.
(iii) The LS equation (1) coincides with the LES equation, if one associates the LS velocity with the filtered velocity and the SS field with fluctuating velocity:

$$\begin{aligned} &\frac{\partial u_i^L}{\partial t} + \frac{\partial}{\partial x_j}\left[u_i^L u_j^L\right]^L = -\frac{\partial p^L}{\partial x_i} + \nu\frac{\partial^2 u_i^L}{\partial x_j^2} - \frac{\partial \tau_{ij}}{\partial x_j} \\ &\tau_{ij} = [u_i^L u_j^S]^L + [u_j^L u_i^S]^L + [u_i^S u_j^S]^L \end{aligned} \tag{5}$$

Note that in Eq. (5), we retain only the LS part of the non-linear term $[u_i^L u_j^L]^L$, instead of $u_i^L u_j^L$, in order to exclude the Leonard stress $[u_i^L u_j^L]^S$ from the residual stress τ_{ij} which leads to a more consistent form of the LES equations [37,38]. Clearly, the Leonard stress is the SS field and does not belong to the class of LS functions $\mathscr{F}^L$, and therefore, it cannot be fully represented on the LS grid.

It is also seen that both the LS equation (1) and the SS equation (2) have the same "symmetric" functional form, and can be obtained one from another by interchanging superscripts L and S. In spite of that, there is a significant physical "asymmetry" that results in different solutions of Eqs. (1) and (2). First, the LS and SS fields are subject to very different boundary conditions as they evolve. Second, the corresponding non-linear product terms $[(u_i^L + u_i^S)(u_j^L + u_j^S)]^L$ and $[(u_i^L + u_i^S)(u_j^L + u_j^S)]^S$ which sustain turbulent energy cascade/backscatter, are acting on different range of scales.

A tendency of LES equations to break down in the near-wall turbulent region (assuming that the "true" LES resolution is employed) is usually attributed to inability to resolve dynamically important near-wall SS structures, since a qualitative reasoning suggests that there are only SS eddies and no LS eddies close to the wall [19]. The production of turbulent kinetic energy attains its maximum level very close to the wall, in the buffer layer, at $y^+ = yu_\tau/\nu \approx 12$ ($u_\tau = \sqrt{\tau/\rho}$ is the friction velocity, τ and ρ are wall shear stress and density), and shows very little variations for a wide range of Reynolds numbers [17]. This creates an extremely difficult problem for subgrid modeling of this region. It requires one to parametrize the residual stress τ_{ij}, which contains product terms involving the high gradient SS velocity, in terms of the LS velocity u_i^L. No satisfactory SGS model has been constructed yet. On the contrary, RANS equations, which employed the same functional form as LES equations, consistently produce better results when they are used as the near-wall model [25], in spite of the fact that they are a priori supposed to resolve much less dynamically important scales and have much more empirical input in the residual (Reynolds) stress models. However, using RANS near-wall models as a part of hybrid LES approach creates many uncertainties on its own. A challenge here is to properly match two types of solutions in the interface region without a loss of structural features of turbulence towards to the wall and retaining an adequate level of the SS fluctuations close to outer LES region [25,29].

In the TLS approach a different strategy is adopted. The SS equation (2) is explicitly used to partially reconstruct the SS dynamics everywhere, including close to the wall.

3. Simplified small-scale equation

In an effort to reduce computational burden, the 3D SS equation (2) is treated on a family of lines Ω_l embedded in the flow domain Ω. As in [16], a collection of orthogonal lines is considered which is depicted in Fig. 1. This leads to the following representation of the SS line velocity fields.

$$u_i^S(\mathbf{x},t) \to u_{i,l_k}^S(l_k,t) = \left\{u_i^S(\mathbf{x},t) | \mathbf{x} \in l_k \subset \Omega\right\}, \quad u_{i,l_k}^S : l_k \times [0,T) \to \mathbb{R}^3 \tag{6}$$

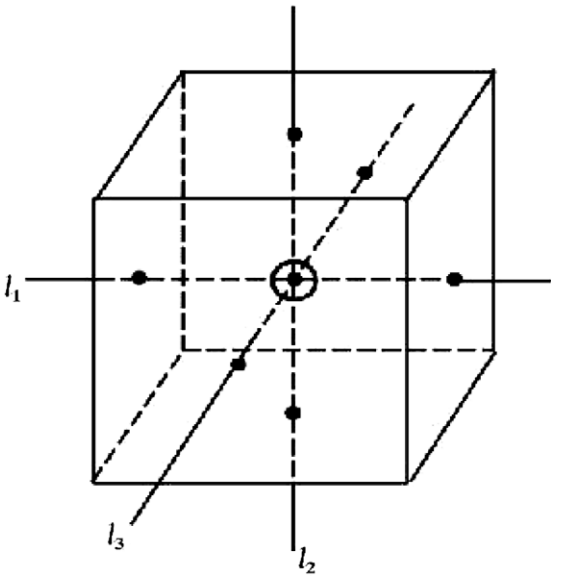

Fig. 1. The SS line arrangement within a LS grid cell.

Here, the SS line velocity u^S_{i,l_k} is defined as the restriction of the SS velocity u^S_i on a one-dimensional subset (smooth manifold) of Ω given by line l_k. To ease further notation, and if there is no possibility of confusion, we drop subscript l_k whenever possible, and use u^S_i or $u^S_i(l_k)$ to denote the SS line velocity.

The following simplified form of the SS equation introduced in [16] is solved on each line $l_k \in \Omega_l$:

$$\frac{\partial u^S_i}{\partial t} + \frac{\partial}{\partial x_j}\left[(u^S_j(l_k) + u^L_j)(u^S_i(l_k) + u^L_i)\right] = 3\nu\frac{\partial^2 u^S_i}{\partial x^2_k} + F^L_i(u^S_j(l_k), u^L_j) \tag{7}$$

where

$$F^L_i(u^S_j(l_k), u^L_j) = \frac{\partial}{\partial x_j}\left[(u^S_j(l_k) + u^L_j)(u^S_i(l_k) + u^L_i)\right]^L$$

The SS velocity fields are then used to explicitly compute the non-linear terms in the LS equation (1) at the LS grid node $\mathbf{x}_n$ according to

$$[u^S_i u^L_j]^L(\mathbf{x}_n, t) \leftarrow \left[u^S_{i,l_k} u^L_{j,l_k}(l_k, t)\right]_{l_k}, \quad [u^S_i u^S_j]^L(\mathbf{x}_n, t) \leftarrow \left[u^S_{i,l_k} u^S_{j,l_k}(l_k, t)\right]_{l_k} \tag{8}$$

Eq. (7) was obtained elsewhere [16] under the following assumptions:

(i) For each SS velocity component u^S_i, the SS second derivative along the line l_k is equal to the averaged sum of the SS second derivatives along all three orthogonal directions:

$$\frac{\partial^2 u^S_i}{\partial x^2_k} = \frac{1}{3}\sum_{j=1}^{3}\frac{\partial^2 u^S_i}{\partial x^2_j}, \quad i,k = 1,2,3 \tag{9}$$

(ii) Changes of the SS part of the convective derivatives of the SS velocity components are neglected in directions transverse ($j \neq k$) to the line l_k:

$$\frac{\partial}{\partial x_j}\left[(u^S_j + u^L_j)(u^S_i + u^L_i)\right]^S = \frac{\partial}{\partial x_j}\left[(u^S_j(l_k) + u^L_j)(u^S_i(l_k) + u^L_i)\right]^S \tag{10}$$

(iii) The SS pressure gradient is neglected, and as a result, the SS continuity constraint is not enforced, i.e., $\partial u^S_j/\partial x_j \neq 0$.

The last requirement is a consequence of adopted numerical approach for the LS integration and the incompressible fluid model. Correspondingly, the incompressibility constraint is used for the LS velocity only, and implemented according to the standard fractional step (projection) method by projecting the intermediate LS velocity onto the space of divergence-free vector fields.

One of the objectives of the present study is to analyze validity of the assumptions (i) and (ii) for a case of non-homogeneous turbulence. Our analysis is based on *a priori* study of DNS data set, which corresponds to fully developed turbulent channel flow simulation of Abe et al. [39]. This DNS study was conducted at $Re_\tau = 640$ ($Re \approx 24{,}300$) on $512 \times 256 \times 256$ orthogonal grid stretched in wall-normal direction. The LS velocity field is computed based on $32 \times 40 \times 32$ LS grid, and then interpolated back on the DNS grid using cubic spline interpolation. The SS velocity field is obtained by subtraction of the LS velocity from the total DNS velocity.

The model assumption (i), Eq. (9), can be expressed as $S_{ik} = 0$, where $S_{ik} = \sum_{j=1}^{3} \partial^2 u_i^S / \partial x_j^2 / 3 - \partial^2 u_i^S / \partial x_k^2$. All nine ($i,k = 1,2,3$) normalized probability density functions (PDF) of S_{ik} are depicted in Fig. 2(b) in logarithmic scale. For comparison, a case of the forced isotropic turbulence [16] is shown in Fig. 2(a). It is seen that all PDFs are collapsed for both cases, and can be fairly well approximated by the same Tsallis distribution [40]. The non-homogeneous case is characterized by wider PDF tails which is consistent with the higher level of turbulence near channel walls. For both cases, the most probable state corresponds to $S_{ik} = 0$. This suggests a certain degree of universality of the assumption for the SS second derivatives. These results are in agreement

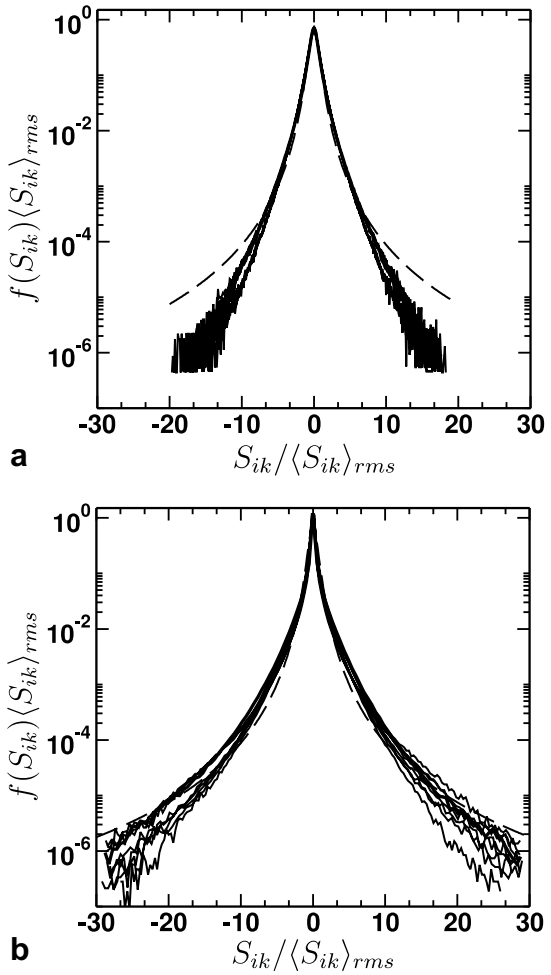

Fig. 2. PDFs of the normalized differences of the second SS derivatives, $S_{ik} = \sum_{j=1}^{3} \partial^2 u_i^S / \partial x_j^2 / 3 - \partial^2 u_i^S / \partial x_k^2$, $i,k = 1,2,3$ compared with the Tsallis distribution (dashed line): (a) forced isotropic turbulence at $Re_\lambda = 140$; (b) turbulent channel flow at $Re_\tau = 640$.

with PDF results for acceleration and pressure gradients obtained in other computational [41] and experimental [42] studies of high-*Re* turbulent flows.

The state $S_{ik} = 0$ corresponds to the events when not only the SS second derivatives in orthogonal directions are small, but also when they are large and approximately equal each other, thus characterizing high gradient, intense turbulent events. This is evident from the joint PDF plots exhibited in Figs. 3–5, where $S_{ik} = 0$ is plotted as a diagonal through I and III quadrants. The highest probable state is attained at the origin.

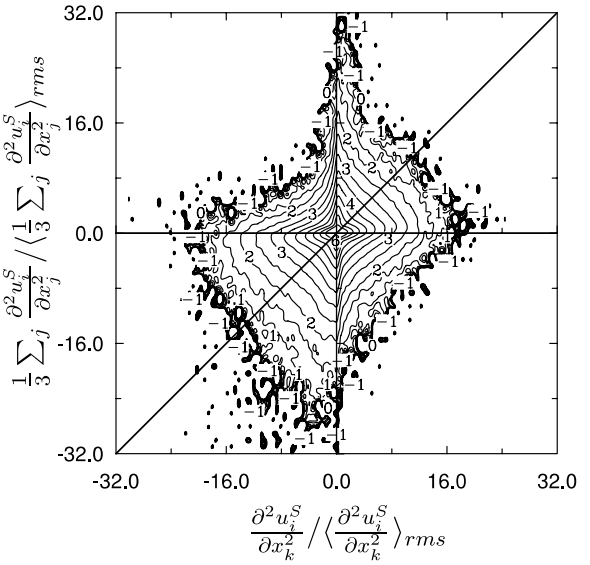

Fig. 3. Contour plots of the logarithm of the joint PDF of the SS second derivative of the longitudinal velocity component ($i = k$, $i = 1$, $k = 1$) and the averaged sum of all SS second derivatives for turbulent channel flow.

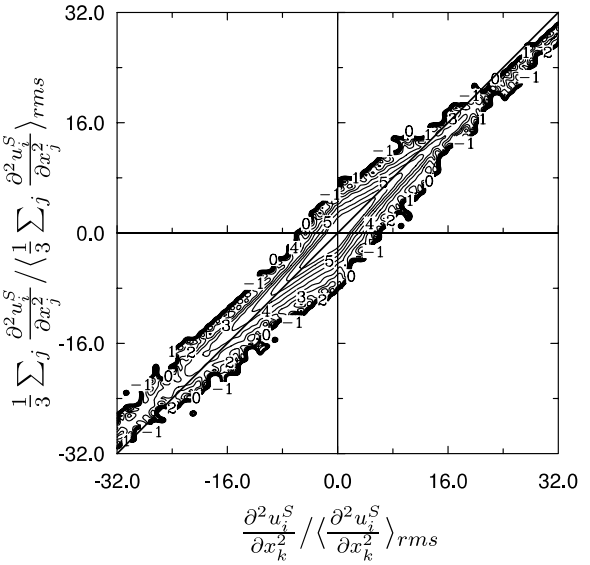

Fig. 4. Contour plots of the logarithm of the joint PDF of the SS second derivative of the transverse velocity component ($i \neq k$, $i = 1$, $k = 2$) and the averaged sum of all SS second derivatives for turbulent channel flow.

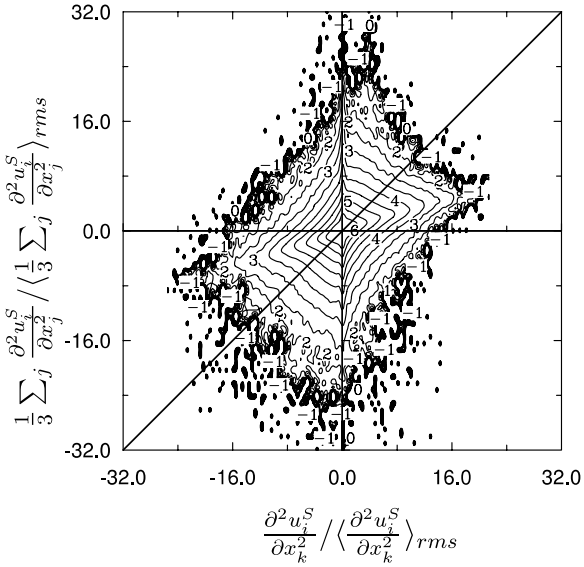

Fig. 5. Contour plots of the logarithm of the joint PDF of the SS second derivative of the transverse velocity component ($i \neq k$, $i = 1$, $k = 3$) and the averaged sum of all SS second derivatives turbulent channel flow.

PDF contour lines exhibit a distorted parallelogram shape somewhat elongated along a diagonal of I and III quadrants suggesting that events described by $S_{ik} = 0$ are highly probable. From Fig. 4, it is seen that the most prominent elongation of the PDF shape exhibits a case of the SS second derivative of streamwise velocity in the wall-normal direction. This is qualitatively consistent with the self-sustaining mechanism of the near-wall turbulence, which is characterized by the bursting process in the wall-normal direction where up to 80% of the Reynolds stress is generated [17]. Fig. 4 also suggests that the assumption (i) is more justified for directions in which the LS derivatives is the largest, i.e., on wall-normal lines.

The fact that, with high probability, and in regions with strong turbulent intensity, the second derivatives of the SS velocity components are large in all three orthogonal directions simultaneously can be qualitatively related to a geometrical picture of the small-scale turbulence. It is known that regions of high level vorticity form non-trivial geometrical pattern which is characterized by elongated vorticity tubes and ribbons called "worms" [43], where high level of energy dissipation is concentrated. A line l_k arbitrarily placed in flow field would intersect low dissipation regions, where all SS second derivatives are small, and also the intense small-scale structures (worms) where the SS dissipation is high. Therefore, the SS second derivatives are expected to be quite large. The intense enstrophy regions (worms) do not necessarily coincide with the high dissipation regions since the high values of the SS derivatives do not always result in the high values of the SS vorticity. However, one can assume that much dissipation is located in the neighborhood of the SS vortex tubes, at the distance not exceeding the order of magnitude of the Kolmogorov scale. This is consistent with the DNS results of Kida [44], as well as with the results based on the simple Burgers vortex model [45].

The joint PDFs of the total and the modeled SS convective terms which correspond to the assumption (ii) are shown in Fig. 6(a)–(c). Since the wall-normal direction plays a special role in the turbulent channel flow, the SS convective derivatives in non-homogeneous direction ($j = 2$) are considered. Three cases, which correspond to different velocity components and the streamwise line l_1 ($k = 1$), are shown. The SS convective derivatives in other directions, streamwise ($j = 1$) and spanwise ($j = 3$), exhibit similar qualitative behavior, and are not shown for brevity. For example, Fig. 6(a) shows a joint PDF of $\partial[(u_2^S + u_2^L)(u_1^S + u_1^L)]^S/\partial x_2$ and $\partial[(u_2^S(l_1) + u_2^L)(u_1^S(l_1) + u_1^L)]^S/\partial x_2$, which are the wall-normal derivative ($j = 2$) of the SS product of streamwise ($i = 1$) and wall-normal ($j = 2$) velocities and its modeled counterpart on streamwise lines ($k = 1$). It is seen that all PDFs attain their maximum value at the origin and have a distorted parallelogram

nal through I and II

e similar effects for a case of non-
otropic urbulence [16]. Namely, they cause
ous dis ation, and to the higher distortion

by the ne arrangement. In this work, we
wn in . While probably not being optim
text LS Cartesian grids. Physically, the
ad cts of the model assumptions (i)
of the SS velocity, which would
se of non-homogeneous turbulent
e gy of the SS velocity field is not
n fe shorter lines positioned with dif-
y app ate the SS field, is beneficial from
angeme ay potentially increase computa-
as well further relaxing the LS resolution
urther st y of physical implications of the
well as the effect of such arrangements on

4. TLS of non-homogeneous turbulence

Two different cases of non-homogeneous turbulent flows are considered: well-developed turbulent channel flow and temporally evolving mixing layers. The primary purpose is to evaluate predictive capabilities of TLS approach to reproduce main features of the wall-bounded turbulent flow, as well as, the free shear-layer flow dominated by LS coherent vortical structures. Flow configurations for both cases are shown in Fig. 7(a) and (b). The coordinates x_1, x_2 and x_3 are chosen to be in streamwise, spanwise and wall-normal (transverse) directions, respectively.

The incremental pressure projection method of van Kan [46] is employed to solve the LS equations. Spatial discretization is done on the staggered grid using finite volume formulation. The convective flux terms are reconstructed using third-order polynomial interpolation. All diffusion terms are computed using second-order central differencing. A third-order, low storage Runge–Kutta scheme is employed for temporal discretization [47] with implicit treatment of diffusion terms in the transverse or wall-normal direction, using Crank–Nicoloson scheme. An explicit, two-step component-wise TVD scheme [48] is employed to numerically integrate the SS equations.

4.1. TLS algorithm and parallelization of SS computations

TLS algorithm consists of the following steps which are performed at mth time level: (i) interpolation of all known LS fields on a system of lines Ω_l (Eq. (6)); (ii) integration of the SS equation (7) on each line l_k starting from zero initial state; (iii) computation of all product terms involving the SS velocity at the LS grid node $\mathbf{x}_n$ (Eq. (8)). The LS equation (1) is then advanced to the next $m+1$ time level [16].

A critical part of TLS calculations is the computational cost of the SS velocity reconstruction on all lines l_k. If the LS grid has resolution of N_i^L points in each coordinate direction x_i, then one needs a system of $N_1^L N_2^L + N_2^L N_3^L + N_1^L N_3^L$ lines. If a SS line has resolution of N_i^S points in the corresponding x_i direction then it translates into additional $N_1^L N_2^L N_3^S + N_2^L N_3^L N_1^S + N_1^L N_3^L N_2^S$ points needed to represent the SS dynamics. Clearly, integration of the SS equation (7) needs to be done in parallel to be computationally viable.

While different strategies are possible to parallelize the SS computations, the master–slave algorithmic model is employed in the present study because of two reasons. First, it gives a simple way of parallel

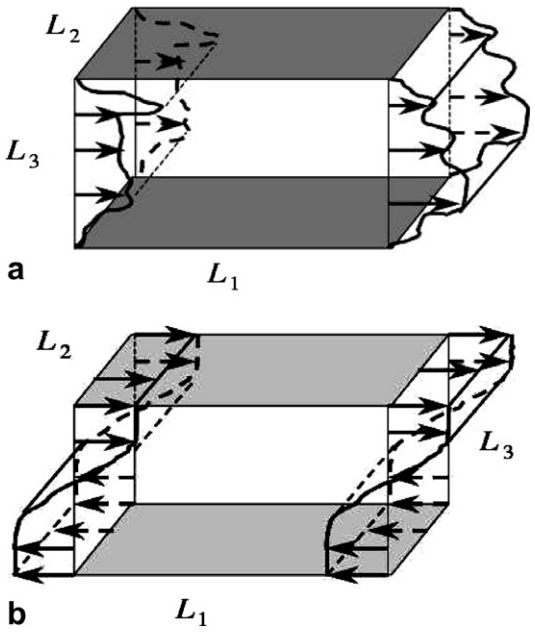

Fig. 7. Sketch of flow configurations: (a) channel flow; (b) temporal mixing layer.

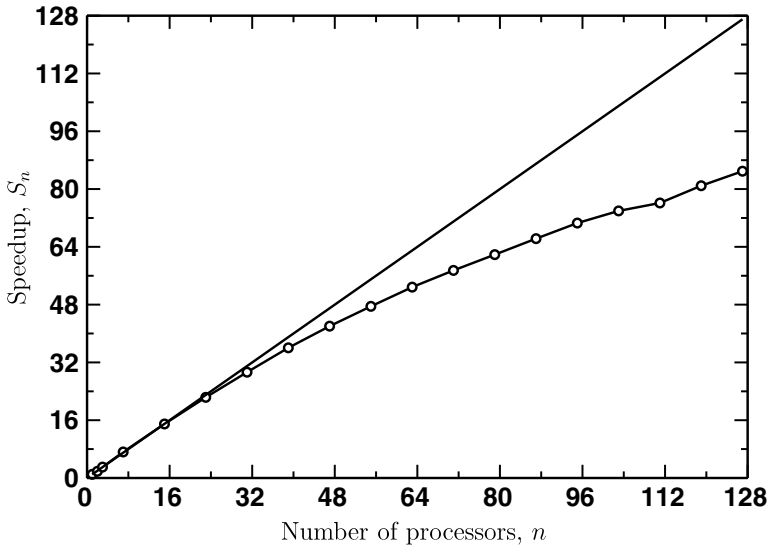

Fig. 8. Speedup of SS computations $S_n = T(1)/T(n)$ compared with linear speedup $S_n = n$.

implementation using message passing interface (MPI) library. Second, the master–slave model provides necessary load balancing for slave processes due to its self-scheduling feature. Thus, for each line l_k, the master process sends all LS fields to a slave process which performs numerical integration of the SS equation (7) and sends the computed SS velocity field back to the master. The master process continues to send new lines to idle slave processes until no lines left, at the same time, the master receives the computed SS line velocities from those slave processes which completed the SS integration.

The parallel performance results of TLS algorithm on IBM eServer Cluster 1600 system are shown in Figs. 8 and 9, for a case of turbulent channel flow at $Re_\tau = 590$. The LS computations were done in serial mode using $32 \times 40 \times 32$ LS grid, as discussed in Section 4.2. Fig. 8 shows parallel speedup curve compared with an ideal linear speedup. Good scalability is observed up to 48–50 processors. As the number of processors grows further, scalability saturation begins to be noticeable. This is due to a possible overload on the master process, since more slave processes need to wait to obtain a next line from the master process to continue computation. Employing several master processes is expected to improve scalability beyond 128 processors.

Wallclock times required for the SS velocity computations between two consecutive LS time steps are shown in Fig. 9. The corresponding LS computation time is depicted as a horizontal line. An estimated time of LES on the same LS grid (which includes ~20–40% overhead due to SGS model [4]) is also shown for comparison. Note that the actual LES time would be significantly higher than the estimated time since typical LES requires at least an order of magnitude higher grid resolution. It is seen, even with one master process employed, the SS computation time becomes less than the LS computation time when more than 98–100 slave processes are used. These results suggest that relaxing the LS grid resolution requirements together with scalable SS computations can provide computational advantageous for TLS approach to treat high-Re number flows.

4.2. Turbulent channel flow

TLS of turbulent channel flow is performed at $Re_\tau = 590$, which corresponds to the reference DNS study of Moser et al. [49]. The Reynolds number $Re_\tau = u_\tau h/\nu$ is based on the friction velocity u_τ and the channel half-width h, and is typically 20–30 times smaller then the centerline velocity Reynolds number $Re = U_0 h/\nu$. The necessity to represent dynamically important near-wall structures leads to the resolution of length scales of size (in wall units) $\Delta x_1^+ \sim O(50)$, $\Delta x_2^+ \sim O(20)$, $\Delta x_3^+ \sim O(1)$ [18,25]. This grid resolution constraint typically

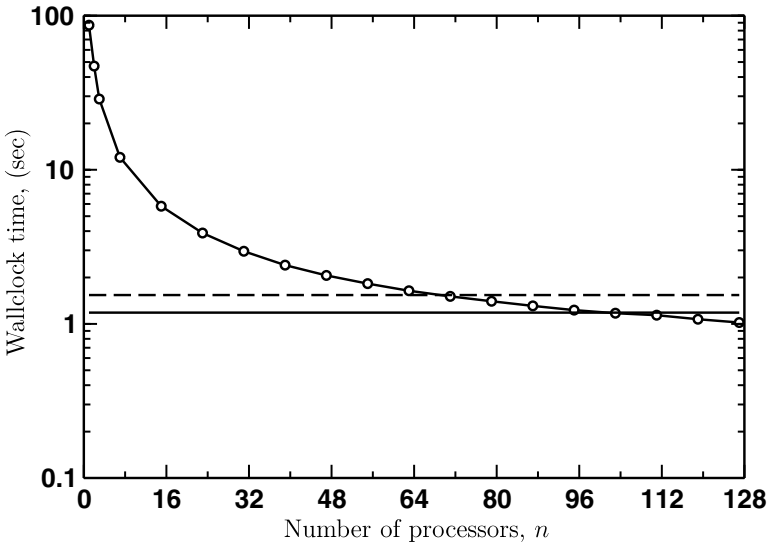

Fig. 9. Wallclock time of SS computations $T(n)$ compared with the time of LS computation (solid line), and an estimated LES time (dashed line), if the same LS grid resolution would have been used.

requires to have several grid points in wall-normal direction below $x_3^+ = 12$, and to maintain the corresponding aspect ratio in spanwise and streamwise directions.

To study the effect of SS velocity on the near-wall LS dynamics the above grid resolution requirements is relaxed significantly. A flow domain of $2\pi \times 2 \times \pi$ is discretized with the LS orthogonal grid of $32 \times 40 \times 32$ cells such that a width of the first near-wall cell is about $\Delta^L x_3^+ \approx 19$. The LS grid is stretched in wall-normal direction, from the wall to the centerline of the channel. As a result, the inner layer is not well resolved and has the near-wall resolution of $\Delta^L x_2^+ \approx 58$ and $\Delta^L x_1^+ \approx 116$ in spanwise and streamwise directions, respectively. Thus, the accurate approximation of the LS turbulent dynamics depends on the correct representation of the SS velocity field in the near-wall region. A uniform SS grid with 256 grid points ($\Delta^S x_2^+ \approx 7.25$ and $\Delta^S x_1^+ \approx 14.5$) is used for lines in the periodic directions. The wall-normal lines are discretized by non-uniform grid with variable number of grid points per LS cell, ranging from 12 near the wall to 4 in the centerline region of the channel, which gives 237 SS grid points with the maximal near-wall resolution of $\Delta^S x_3^+ \approx 1.58$. As a result, most near-wall dynamics is expected to be resolved on the near-wall lines. The periodic boundary conditions are used for all lines in streamwise and spanwise directions while the no-slip boundary conditions are adopted for the wall-normal lines.

To accumulate flow data for statistical analysis the turbulent stationary state has to be reached during the course of simulations. The time evolution of the LS and the SS turbulent kinetic energies is shown in Fig. 10. After initial transient period both the LS and the SS fields reach the stationary state at time $T \approx 6$. The SS turbulent kinetic energy E^S is computed by averaging of $u_i^S u_i^S/2$ over all SS lines. The values of the SS turbulent kinetic energy is multiplied by 150 to make visual comparison possible. The SS turbulent kinetic energy follows the pattern similar to the LS energy, however it is characterized by more intermittent, high-frequency fluctuations related to high gradient, non-Gaussian SS events captured by the SS field.

Some qualitative information on the SS model behavior can be drawn from analysis of the SS velocity field on lines. The streamwise LS and SS velocity components along three different streamwise and spanwise lines are given in Figs. 11 and 13. The lines are chosen in the following manner: near the wall ($x_3^+ = 9.4$), close to the centerline ($x_3^+ = 373$), and in the intermediate region between the wall and the centerline ($x_3^+ = 138$). Note that profiles for the near-center line and the intermediate line SS velocities are shifted upwards from zero to enable comparison. The corresponding line energy spectra are shown in Figs. 12 and 14, respectively. These plots show that the intensity and the spectral energy content of the SS velocity are increasing toward the wall. The SS energy spectra are approximately matched with the corresponding LS energy spectra showing almost the same energy content at the smallest resolved LS level. The instantaneous profiles of the LS and

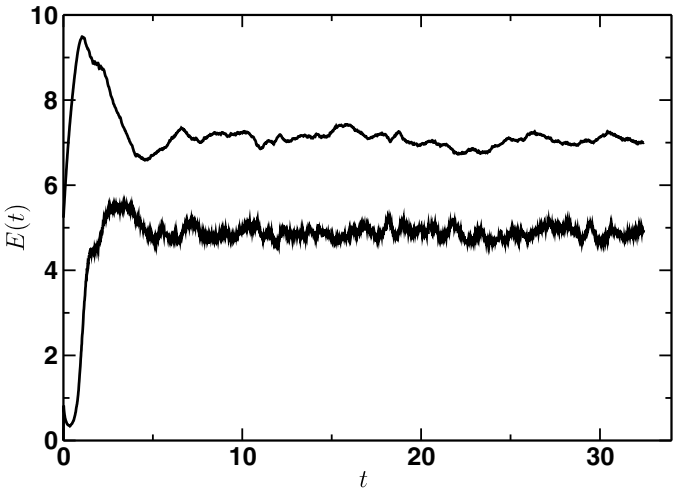

Fig. 10. Time evolution of the LS (upper line) and the SS (lower line) turbulent kinetic energies. The SS energy $E^S(t)$ is multiplied by 150 to enable comparison.

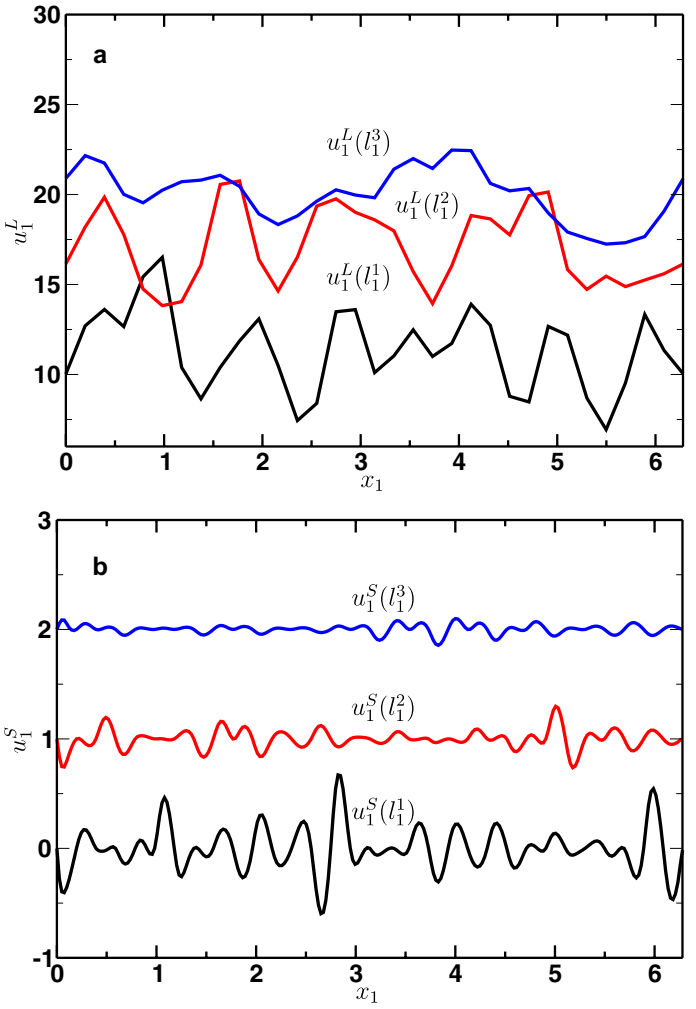

Fig. 11. Typical instantaneous velocity profiles along streamwise lines at $x_3^+ = 9.4$, $x_3^+ = 138$, $x_3^+ = 373$: (a) LS streamwise velocity u_1^L; (b) SS streamwise velocity u_1^S. Two upper profiles of the SS velocity are shifted upwards by 1 and 2 respectively.

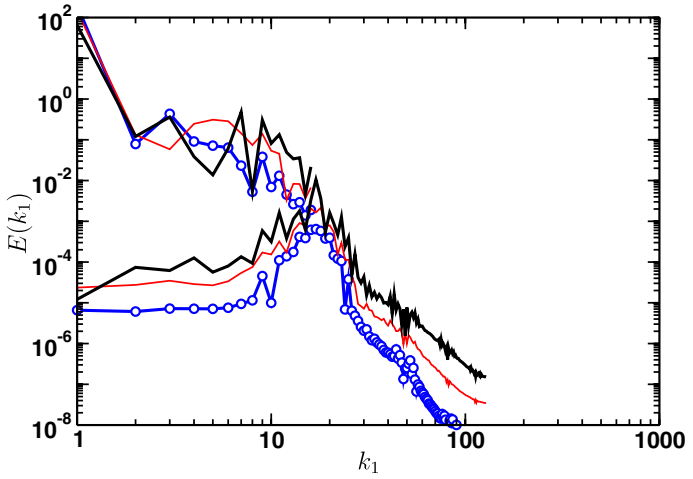

Fig. 12. LS and SS line energy spectra for streamwise lines located at $x_3^+ = 9.4$ (thick solid line), $x_3^+ = 138$ (thin solid line), $x_3^+ = 373$ (circles).

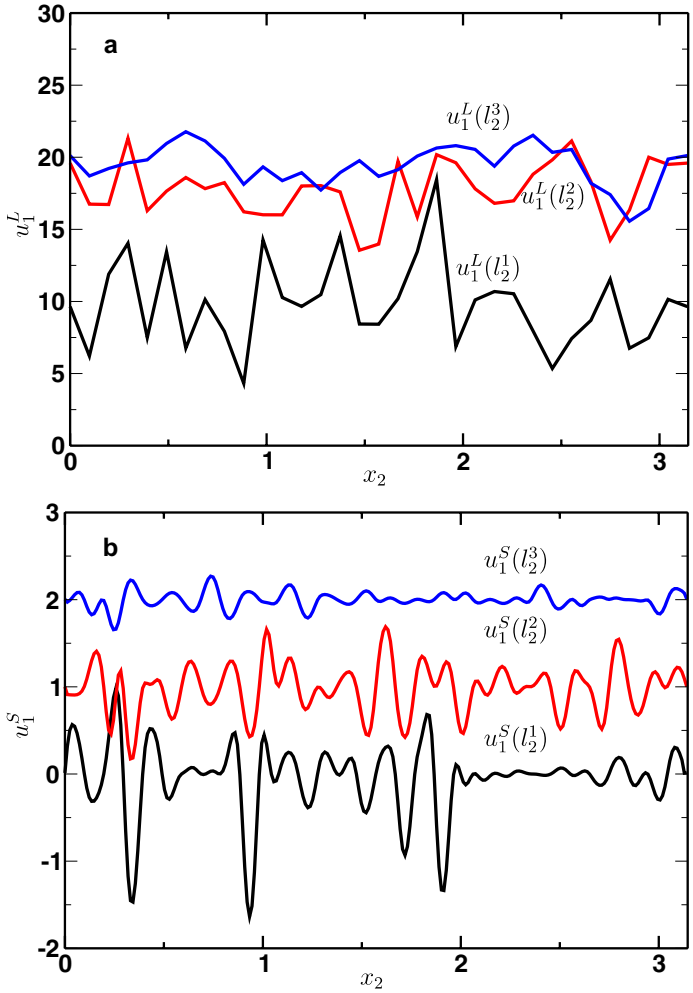

Fig. 13. Typical instantaneous velocity profiles along spanwise lines at $x_3^+ = 9.4$, $x_3^+ = 138$, $x_3^+ = 373$: (a) LS streamwise velocity u_1^L; (b) SS streamwise velocity u_1^S. Two upper profiles of the SS velocity are shifted upwards by 1 and 2 respectively.

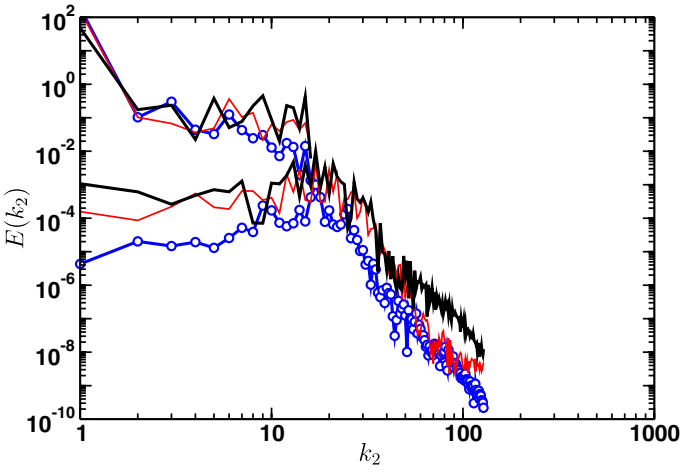

Fig. 14. LS and SS line energy spectra for spanwise lines located at $x_3^+ = 9.4$ (thick solid line), $x_3^+ = 138$ (thin solid line), $x_3^+ = 373$ (circles).

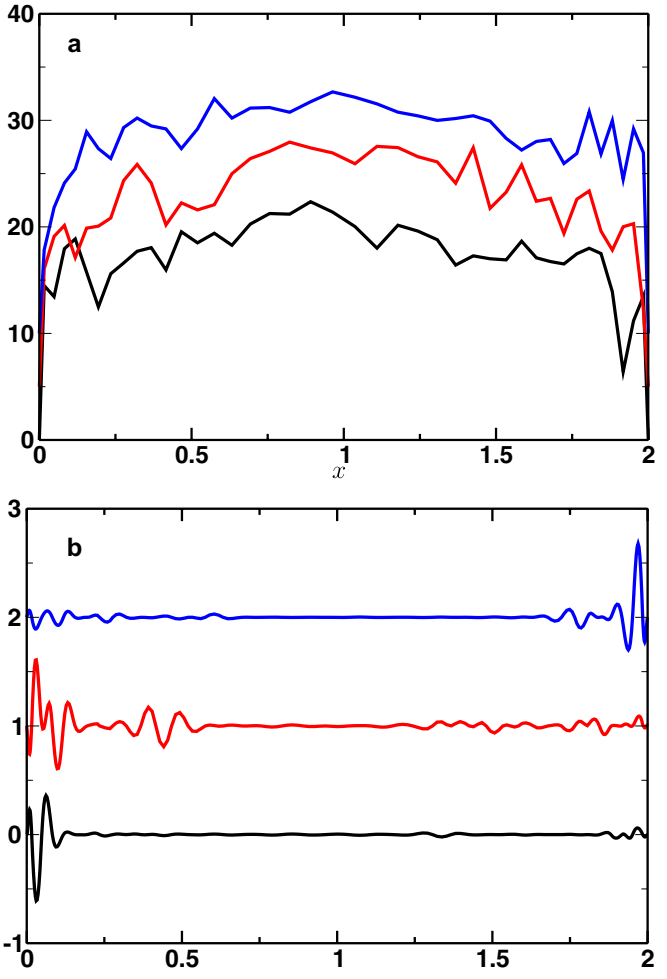

respectively. The contours of the LS spanwise vorticity for Case 1 (Fig. 22(a), (c) and (e)) exhibit the rollup, the pairing and the post-pairing stages of the mixing layer development. During the pairing, two well-developed vortices generated by the rollup of the fundamental mode come together and merge to form a new bigger vortex core. The contour plots of the SS spanwise vorticity are shown in Fig. 22(b), (d) and (f), and

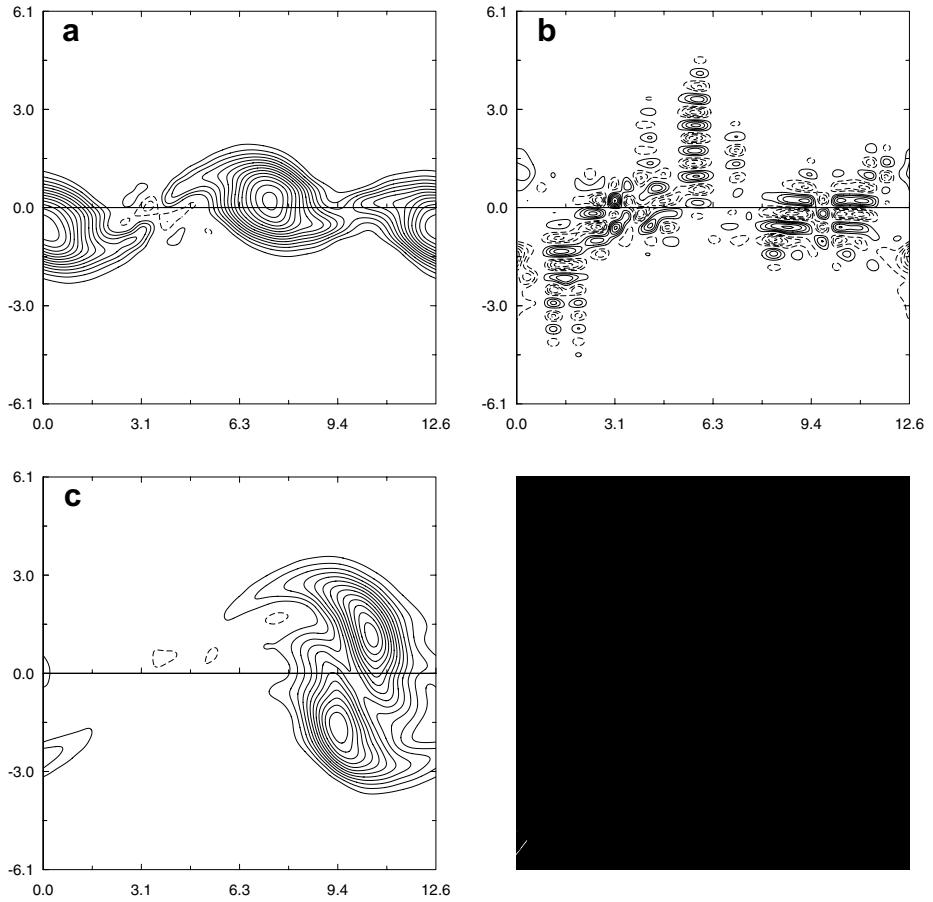

demonstrate clusters of small counter-rotating vortices which exist in high gradient regions of the LS spanwise vorticity. The peak intensities of the SS spanwise vorticity steadily decrease as the LS two-dimensional vortical structures develop, absorbing energy from the SS field. At $T^{\mathrm{I}} = 184$ the maximum (minimum) value of the SS spanwise vorticity is 2.07 (-2.32), respectively, and is down from the corresponding values of 2.52 (-2.72) at

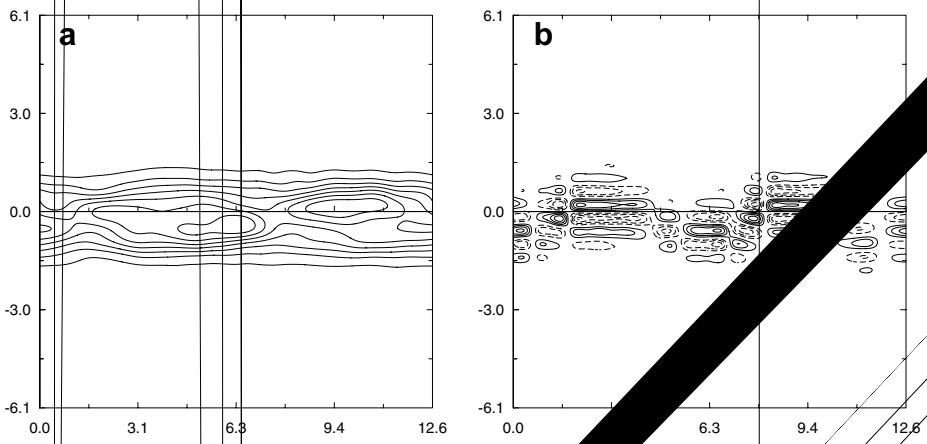

$T^{\mathrm{I}} = 36$. In Case 2, the SS vortices are still created in regions where the large spatial changes of the LS vorticity are dominant, as shown in Fig. 23(b), (d) and (f). However, the peak intensities of the SS spanwise vorticity constantly grows from $\max(\omega_2^S) = 1.69$ $(\min(\omega_2^S) = -1.95)$ at $T^{\mathrm{II}} = 323$ to $\max(\omega_2^S) = 4.46$ $(\min(\omega_2^S) = -4.46)$ at $T^{\mathrm{II}} = 560$, suggesting the forward cascade of energy from the LS to the SS as the three-dimensional modes prevail and the flow loses its initial two-dimensional structure and becomes completely turbulent.

The qualitative difference between the LS vortical structures in Case 1 and Case 2 is further evident if one considers the second invariant of the velocity-gradient tensor which is often used to identify vortex regions which exhibit significant rotational motions. Positive values of the second invariant of the velocity-gradient tensor $Q > 0$ indicate the regions of intense enstrophy (rotation) and weak shear [54]. The LS and the SS second invariants of $\partial u_i^L/\partial x_j$ and $\partial u_i^S/\partial x_j$ are $Q^L = (\Omega_{ij}^L\Omega_{ij}^L - S_{ij}^L S_{ij}^L)/2$, $Q^S = (\Omega_{ij}^S\Omega_{ij}^S - S_{ij}^S S_{ij}^S)/2$, where Ω_{ij}^L, Ω_{ij}^S and S_{ij}^L, S_{ij}^S are the rate-of-rotation and rate-of-strain tensors of the LS and SS fields respectively, and defined as $\Omega_{ij}^{L,S} = (\partial u_i^{L,S}/\partial x_j - \partial u_j^{L,S}/\partial x_i)/2$, $S_{ij}^{L,S} = (\partial u_i^{L,S}/\partial x_j + \partial u_j^{L,S}/\partial x_i)/2$.

Isosurfaces of the second invariant of the LS and the SS velocity-gradient tensors for both Cases are exhibited in Figs. 24 and 25, respectively. The positive regions of the LS invariant Q^L are shown at two levels equal to 0.12 and 11.0. Fig. 24(a) demonstrates the basic 3D structure in the mixing layers. Pairing of two spanwise vortices is highlighted by the isosurface of the higher value of Q^L. In mixing layers, two-dimensional LS structures are subject to three-dimensional instabilities, which is manifested by existence of counter-rotating streamwise "rib" vortices, and have been studied extensively in the past [51]. This structure is clearly visualized by lower value of Q^L.

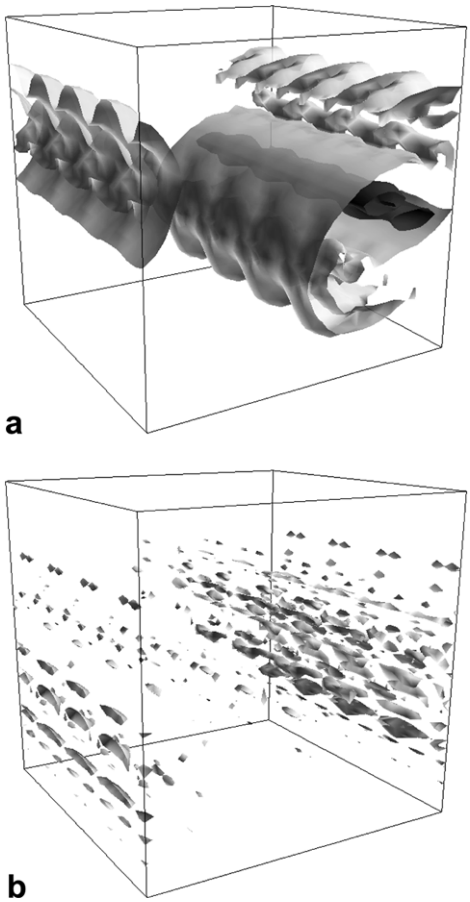

Fig. 24. (a) Isosurfaces of the second invariant $Q^L = 0.12$ (light, transparent) and $Q^L = 11$ (dark) at $T = 147$; (b) isosurfaces of the second invariant $Q^S = 0.12$ at $T = 147$.

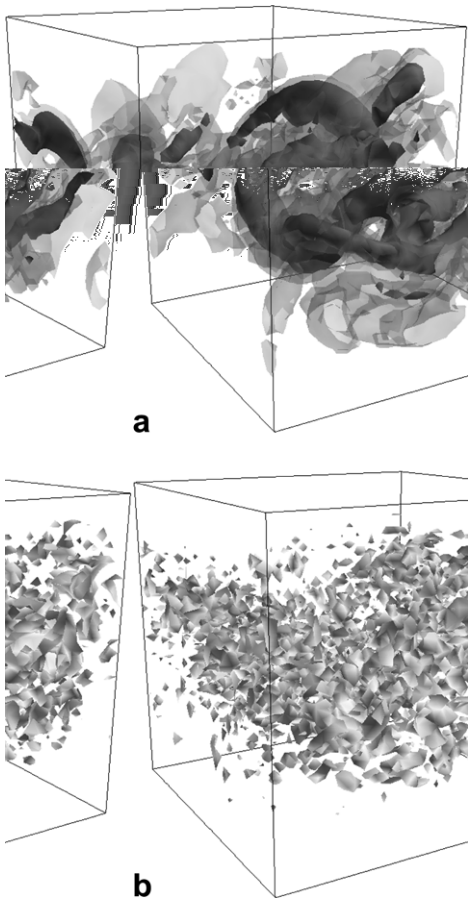

Fig. 25. (a) Isosurfaces of the second invariant $Q^L = 0.12$ (light, transparent) and $Q^L = 11$ (dark) at $T = 560$; (b) isosurfaces of the second invariant $Q^S = 0.12$ at $T = 560$.

Fig. 25(a) shows the LS vortical structure for the Case 2 at later time $T^{II} = 560$, when the two-dimensional subharmonic and the counter-rotating streamwise vortices are already significantly distorted. These LS vortical structures strongly affect the corresponding SS field. In Case 1 (Fig. 24(b)), the SS invariant exhibits an approximate, quasi-two-dimensional pattern, while Case 2 is characterized by almost structureless, random SS vorticity regions, as shown in Fig. 25(b).

Finally, turbulent statistics is examined to determine whether the development of the mixing layer reaches the self-similar stage. The well-known property of the turbulent mixing layer is the self-similar evolution after an initial transient stage, provided that there is a sufficiently large computational domain and the Reynolds number is high [55]. The self-similarity regime is usually characterized by the linear growth of the layer momentum thickness in time, and by coinciding profiles of the normalized turbulent intensities for different times (or downstream locations for spatially evolving mixing layers).

However, the non-dimensional times of the beginning and the end of the self-similar regime are strongly depend in the initial conditions which makes the meaningful comparison of experimental and numerical (DNS or LES) results difficult. The experimental and numerical studies [56,57] suggest that the turbulent statistics, as well as the flow structure are strongly affected by the initial conditions and the computational domain size. Significant differences exist in all stages of the mixing layer development including the self-similar regime leading to multiple, non-unique self-similar states [57]. As a result, any validating conclusions drawn on routinely compared data from the different numerical (DNS or LES) and experimental configurations are based on implicit assumption of the unique self-similar state, and therefore, should be taken with caution.

Nevertheless, despite the significant difference in the initial conditions, it is instructive to compare qualitatively the TLS results of Case 2 with existing DNS [55] and experimental results [58]. A Galerkin spectral method was employed in the DNS with resolution of $512 \times 210 \times 192$ modes and the initial vorticity thickness Reynolds number Re_ω of 1370. Initial velocity field was generated by bringing together two turbulent boundary layer realizations with their respective free streams moving in opposite directions. In the experimental work [58], a mixing layer originated from two tripped splitter-plate boundary layers.

Fig. 21 shows that the evolution of the momentum thickness is not fully linear in the turbulent regime, except for a small time interval around $T^{\mathrm{II}} = 500$. However, the exact estimation of the starting point of the self-similarity is difficult. The momentum thickness is based on integration of the mean LS velocity. As a result numerical estimations that are based on the explicit calculation of the momentum thickness higher derivatives bear an unavoidable degree of arbitrariness. More transparent estimation can be obtained by considering evolution of statistical quantities such as the integrated dissipation or the resolved turbulent kinetic energy $E^L = \langle u_i^{L'} u_i^{L'} \rangle / 2$ at $x_3 = 0$, which should not depend on time during the self-similar period

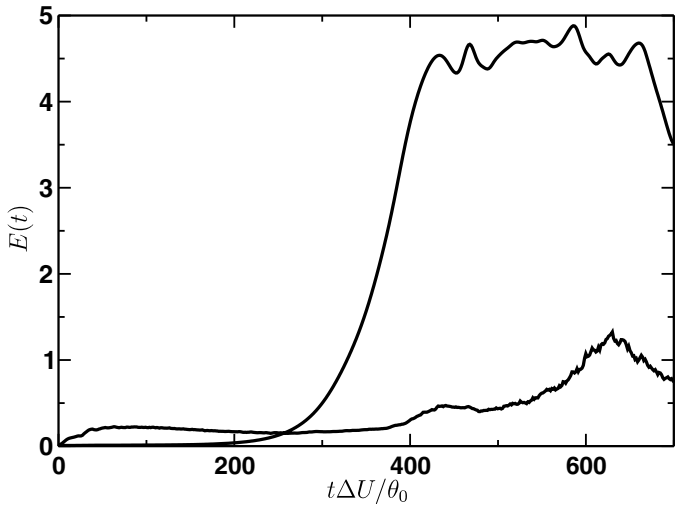

Fig. 26. Evolution of the LS $E^L(t)$ (upper line) and the SS $E^S(t)$ (lower line) turbulent kinetic energies at $x_3 = 0$. $E^S(t)$ is multiplied by 20 to enable comparison.

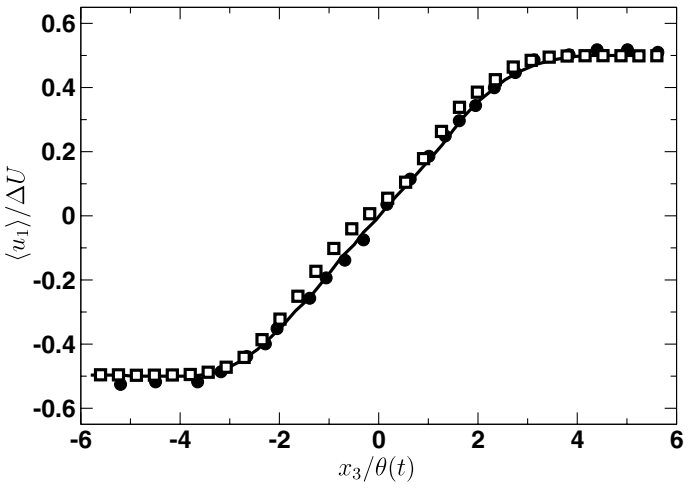

Fig. 27. Space-averaged LS streamwise velocity at $T = 510$ (open squares) compared with the mean streamwise velocity for the self-similar state obtained in DNS (line) [55] and experimental studies (circles) [58].

[11]. Here, $u_i^{L'}$ denotes the fluctuating LS velocity field. Time evolution of the LS and the SS turbulent kinetic energies at $x_3 = 0$ are shown in Fig. 26. It appears that an approximate self-similar regime is reached for the non-dimensional times greater then 460. Note that the corresponding SS turbulent kinetic energy, computed as the total SS energy averaged over the lines belonging to $x_3 = 0$ plane, also demonstrates the similar trend until about $T^{II} = 530$. Due to the finite size of the computational domain the statistics eventually decay.

Space-averaged mean velocity profile is shown in Fig. 27 and agrees well with DNS and experimental results. Fig. 28 demonstrates RMS of the LS velocity fluctuations. Despite very different initial conditions adopted in both DNS and experimental studies, as well as the coarse LS resolution of the TLS case, the turbulent intensities of the LS field show qualitatively good agreement with DNS and experimental results. Some differences in predicting peak values of the turbulent intensities may be also attributed to insufficient statistical sample due to the limited and approximate existence of the self-similar stage. Here, the role of

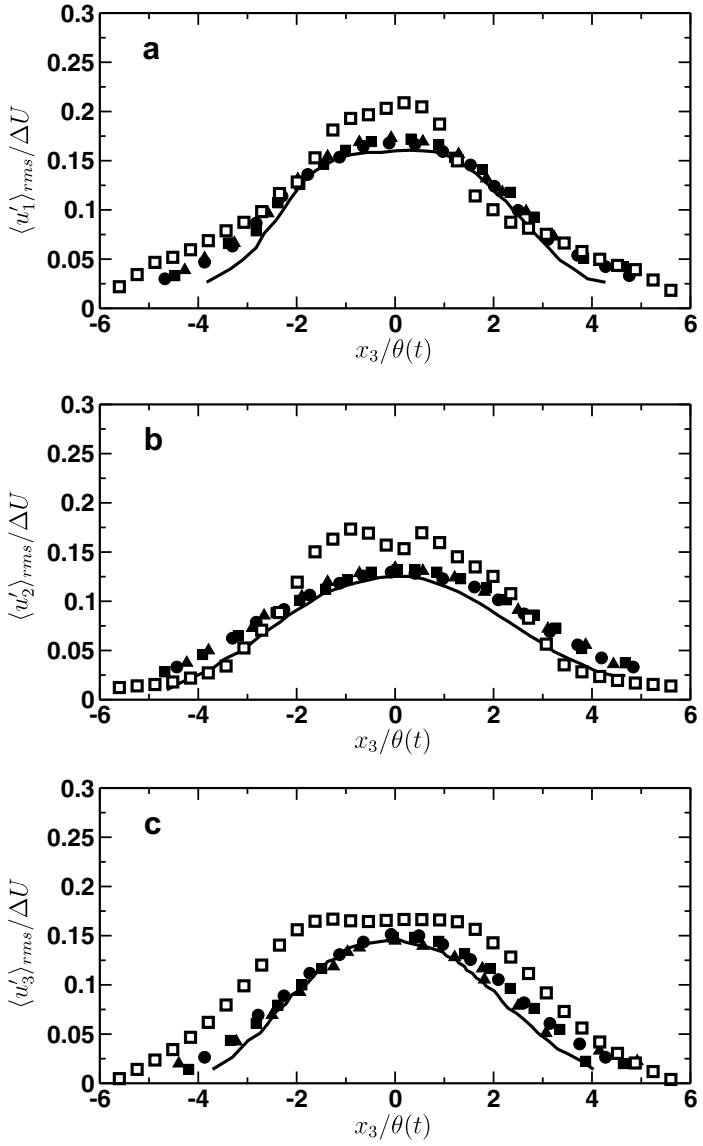

Fig. 28. Space-averaged LS rms velocities at $T = 510$ (open squares): streamwise (a), spanwise (b), normal (c), compared with the rms velocities for the self-similar state obtained in DNS (line) and experimental studies (symbols).

the computational domain is particular important. As reported by Balaras et al. [57], who recently conducted the high resolution LES study of the self-similar regimes in turbulent mixing layers, the combined effect of different initial conditions and domain sizes can result in up to 83% difference in predicting peak values of turbulent intensities, where the spanwise velocity component is the most affected.

Overall, these results suggest that the SS velocity field generated by the simplified SS equation (7) is capable of capturing physically relevant details of turbulent flow pattern in the presence of the LS coherent structures, which makes the TLS approach feasible for extension to treat complex, massively separated flows.

5. Conclusion

Two level simulation (TLS) approach, which is based on the simultaneous consideration of the LS and the SS equations, has been extended to treat two benchmark cases of simple non-homogeneous turbulent flows, well-developed turbulent channel flow and temporally evolving mixing layers. While the LS equation is simulated on a coarse grid, the SS equation is simplified and solved, with much higher resolution, on lower-dimensional domain representing a collection of orthogonal lines embedded in 3D flow domain. Explicitly known SS velocity provides the closure for the LS equations, thus allowing to avoid an eddy-viscosity type of modeling.

Implications of the SS model assumptions have been studied based on *a priori* analysis of DNS data for turbulent channel flow and have shown similarities with the previous analysis of forced isotropic turbulence data [16]. This suggests some degree of universality of the simplified SS equation, and its possible applicability for more geometrically complex non-homogeneous turbulent flows.

Fully coupled simulations of the test cases demonstrate a good capability to predict essential turbulent flow features irrespective to a mechanism of turbulence production. Explicit accounting of the SS motion proved to be beneficial for predicting the LS dynamics in turbulent channel flow. While a size of the wall-adjacent cell ($x_3^+ \approx 19$, at $Re_\tau = 590$) shows improvement in comparison with LES resolution requirements, it is still less than the minimal allowable size ($x_3^+ > 100$–200) which would make computations affordable for practically relevant Reynolds numbers. Important question of how coarse the LS resolution can be to sustain an acceptable level of the SS velocity fluctuations, and how it varies with Reynolds number require further research. It is clear that too coarse representation of the LS field may diminish the LS velocity gradients which can adversely affect the reconstructed SS velocity field near the wall.

Acknowledgements

The authors are grateful to Hiroshi Kawamura for providing DNS data sets of turbulent channel flow. This work has been supported by the Office of Naval Research (Program Manager Dr. Ronald Joslin). Computational time has been provided by NAVO MSRC.

References

[1] A. Leonard, Energy cascade in large-eddy simulations of turbulent fluid flows, Advances in Geophysics A 18 (1974) 237–248.
[2] P. Sagaut, Large Eddy Simulation for Incompressible Flows: An Introduction, Springer, 2001.
[3] C. Meneveau, J. Katz, Scale-invariance and turbulence models for large-eddy simulation, Annual Review of Fluid Mechanics 32 (2000) 1–32.
[4] U. Piomelli, Large-eddy simulation: achievements and challenges, Progress in Aerospace Science 35 (1999) 335–362.
[5] R.A. Clark, J.H. Ferziger, W.C. Reynolds, Evaluation of subgrid-scale models using an accurately simulated turbulent flow, Journal of Fluid Mechanics 91 (1979) 1–16.
[6] M. Germano, U. Piomelli, P. Moin, W.H. Cabot, A dynamic subgrid-scale eddy viscosity model, Physics of Fluids A 3 (1991) 1760–1765.
[7] C. Meneveau, T. Lund, W. Cabot, A Lagrangian dynamic subgrid-scale model of turbulence, Journal of Fluid Mechanics 319 (1996) 353–385.
[8] J.A. Domaradzki, E.M. Saiki, A subgrid-scale model based on the estimation of unresolved scales of turbulence, Physics of Fluids 9 (1997) 2148–2164.
[9] S. Stolz, N.A. Adams, L. Kleiser, An approximate deconvolution model for large-eddy simulation with application to incompressible wall-bounded flows, Physics of Fluids 13 (2001) 997–1015.
[10] C. Fureby, G. Tabor, H.G. Weller, A.D. Gosman, A comparative study of subgrid scale models in homogeneous isotropic turbulence, Physics of fluids 9 (1997) 1416–1429.

[11] B. Vreman, B. Geurts, H. Kuerten, Large-eddy simulation of the turbulent mixing layers, Journal of Fluid Mechanics 339 (1997) 357–390.
[12] F. Sarghini, U. Piomelli, E. Balaras, Scale-similar models for large-eddy simulations, Physics of Fluids 11 (1999) 1596–15607.
[13] P. Moin, Advances in large eddy simulation methodology for complex flows, International Journal of Heat and Fluid Flow 23 (2002) 710–720.
[14] W. Rodi, DNS and LES of some engineering flows, Fluid Dynamics Research 38 (2006) 145–173.
[15] S.B. Pope, Ten questions concerning the large-eddy simulation of turbulent flows, New Journal of Physics 6 (2004) 35.
[16] K.A. Kemenov, S. Menon, Explicit small-scale velocity simulation for high-*Re* turbulent flows, Journal of Computational Physics (2006), in press, doi:10.1016/j.jcp.2006.05.006.
[17] R.L. Panton, Overview of the self-sustaining mechanisms of wall turbulence, Progress in Aerospace Science 37 (2001) 341–383.
[18] D.R. Chapman, Computational aerodynamics, development and outlook, AIAA Journal 17 (1979) 1293–1313.
[19] U. Piomelli, E. Balaras, Wall layer models for large eddy simulation, Annual Review of Fluid Mechanics 34 (2002) 349–374.
[20] U. Schumann, Subgrid scale model for finite difference simulations of turbulent flows in plane channels and annuli, Journal of Computational Physics 18 (1975) 376–404.
[21] G. Grötzbach, Direct and large eddy simulation of turbulent channel flows, in: Encyclopedia of Fluid Mechanics, Gulf Publishing, West Orange, NJ, 1987, pp. 1337–1391.
[22] U. Piomelli, P. Moin, J.H. Ferziger, J. Kim, New approximate boundary conditions for large-eddy simulations of wall-bounded flows, Physics of Fluids A 1 (1989) 1061–1068.
[23] E. Balaras, C. Benocci, U. Piomelli, Two-layer approximate boundary conditions for large-eddy simulations, AIAA Journal 34 (1996) 1111–1119.
[24] P.R. Spalart, W.H. Jou, M. Strelets, S.R. Allmaras, Comments on feasibility of LES for wings and on a hybrid RANS/LES approach, in: Advances in DNS/LES, Greyden Press, 1997, pp. 137–147.
[25] L. Temmerman, M. Hadžiabdić, M.A. Leschziner, K. Hanjalić, A hybrid two-layer URANS-LES approach for large eddy simulation at high Reynolds numbers, International Journal of Heat and Fluid Flow 26 (2005) 173–190.
[26] N.V. Nikitin, F. Nicoud, B. Wasistho, K.D. Squires, P.R. Spalart, An approach to wall modeling in large eddy simulations, Physics of Fluids 12 (2000) 1629–1632.
[27] U. Piomelli, E. Balaras, H. Pasinato, K.D. Squires, P.R. Spalart, The inner–outer layer interface in large-eddy simulations with wall-layer models, International Journal of Heat and Fluid Flow 24 (2003) 538–550.
[28] Y. Benarafa, O. Cioni, F. Ducros, P. Sagaut, RANS/LES coupling for unsteady turbulent flow simulation at high Reynolds number on coarse meshes, Computer Methods in Applied Mechanics and Engineering 195 (2006) 2939–2960.
[29] F. Hamba, A hybrid RANS/LES simulation of high-Reynolds-number channel flow using additional filtering at the interface, Theoretical and Computational Fluid Dynamics 20 (2006) 89–101.
[30] R. Schmidt, A. Kerstein, S. Wunsch, V. Nilsen, Near-wall LES closure based on one-dimensional turbulence modeling, Journal of Computational Physics 186 (2003) 317–355.
[31] A.R. Kerstein, One-dimensional turbulence: model formulation and application to homogeneous turbulence, shear flows and buoyant stratified flows, Journal of Fluid Mechanics 392 (1999) 277–334.
[32] E. Tadmor, Convergence of spectral methods for nonlinear conservation laws, SIAM Journal of Numerical Analysis 26 (1989) 30–44.
[33] G.-S. Karamanos, G.E. Karniadakis, A spectral vanishing viscosity method for large-eddy simulations, Journal of Computational Physics 163 (2000) 22–50.
[34] R.M. Kirby, G.E. Karniadakis, Coarse resolution turbulence simulations with spectral vanishing viscosity – large-eddy simulations (SVV-LES), Journal of Fluids Engineering 124 (2002) 886–891.
[35] C. Fureby, F.F. Grinstein, Large eddy simulation of high-Reynolds-number free and wall-bounded flows, Journal of Computational Physics 181 (2002) 68–97.
[36] F.F. Grinstein, C. Fureby, Recent progress on MILES for high Reynolds number flows, Journal of Fluids Engineering 124 (2002) 848–861.
[37] T. Lund, The use of explicit filters in large eddy simulation, Computers & Mathematics with Applications 46 (2003) 603–616.
[38] G. De Stefano, O.V. Vasilyev, "Perfect" modeling framework for dynamic SGS model testing in large eddy simulation, Theoretical and Computational Fluid Dynamics 18 (2004) 27–41.
[39] H. Abe, H. Kawamura, Y. Matsuo, Direct numerical simulation of a fully developed turbulent channel flow with respect to the Reynolds number dependence, ASME Journal of Fluids Engineering 123 (2001) 382–393.
[40] C. Beck, Superstatistics in hydrodynamic turbulence, Physica D 193 (2004) 195–207.
[41] T. Gotoh, R. Kraichnan, Turbulence and Tsallis statistics, Physica D 193 (2004) 231–244.
[42] G.A. Voth, A. La Porta, A.M. Crawford, J. Alexander, E. Bodenschatz, Measurements of particle accelerations in fully developed turbulence, Journal of Fluid Mechanics 469 (2002) 121–160.
[43] J. Jimenez, A.A. Wray, P.G. Saffman, R.S. Rogallo, The structure of intense vorticity in isotropic turbulence, Journal of Fluid Mechanics 255 (1993) 65–90.
[44] S. Kida, Vortical structure of turbulence, in: Mechanics for a New Millennium, Kluwer Academic Press, 2001, pp. 445–456.
[45] P.A. Davidson, Turbulence: An Introduction for Scientists and Engineers, Oxford University Press, 2004.
[46] J. van Kan, A second-order accurate pressure-correction scheme for viscous incompressible flow, SIAM Journal of on Scientific and Statistical Computing 7 (1986) 870–891.
[47] J.H. Williamson, Low-storage Runge–Kutta schemes, Journal of Computational Physics 35 (1980) 48–56.

[48] H. Yu, Y. Liu, A second order accurate, component-wise TVD scheme for nonlinear, hyperbolic conservation laws, Journal of Computational Physics 173 (2001) 1–16.
[49] R. Moser, J. Kim, N. Mansour, Direct numerical simulation of turbulent channel flow up to $Re_\tau = 590$, Physics of Fluids 11 (1999) 943–945.
[50] A. Michalke, On the inviscid instability of the hyperbolic tangent velocity profile, Journal of Fluid Mechanics 19 (1964) 543–556.
[51] R.W. Metcalfe, S.A. Orszag, M.E. Brachet, S. Menon, J.J. Riley, Secondary instability of a temporally growing mixing layer, Journal of Fluid Mechanics 184 (1987) 207–243.
[52] R. Moser, M.M. Rogers, The three-dimensional evolution of a plane mixing layer: pairing and transition to turbulence, Journal of Fluid Mechanics 247 (1993) 275–320.
[53] W. Ling, J. Chung, T.R. Troutt, C.T. Crowe, Direct numerical simulation of a three-dimensional temporal mixing layer with particle dispersion, Journal of Fluid Mechanics 358 (1998) 61–85.
[54] J. Zhou, R.J. Adrian, S. Balachandar, T.M. Kendall, Mechanisms for generating coherent packets of hairpin vortices, Journal of Fluid Mechanics 387 (1999) 353–396.
[55] M.M. Rogers, R.D. Moser, Direct simulation of a self-similar turbulent mixing layer, Physics of Fluids 6 (1994) 903–923.
[56] G.L. Dimotakis, G.L. Brown, The mixing layer at high Reynolds number: large-structure dynamics and entrainment, Journal of Fluid Mechanics 78 (1976) 535–560.
[57] E. Balaras, U. Piomelli, J.M. Wallace, Self-similar states in turbulent mixing layers, Journal of Fluid Mechanics 446 (2001) 1–24.
[58] J.H. Bell, R.D. Mehta, Development of a two-stream mixing layer from tripped and untripped boundary layers, AIAA Journal 28 (1990) 2034–2042.